《報文》 HWAHAK KONGHAK Vol. 19, No. 2, April 1981, pp. 107—120
(Journal of the Korean Institute of Chemical Engineers)

회전 원통을 통과하는 기체의 유동

박 흥 목·장 호 남

한국과학원 화학공학과

윤 창 구

한국과학기술연구소 화학공정연구실

(접수 1981. 3. 7)

Source-Sink Flows in a Rotating Cylinder

Hung Mok Park and Ho Nam Chang

Department of Chemical Engineering,
Korea Advanced Institute of Science, Seoul 131, Korea.

C. K. Yun

Chemical Process Laboratory,
Korea Institute of Science and Technology, Seoul 130, Korea

(Received March 7, 1981)

요 약

회전하는 실린더의 양끝 덮개에 원형의 slit 상의 source와 sink가 있는 경우, 그 유동을 수치해석적으로 모사하였다. 반경 방향으로 밀도의 분포를 반경의 함수로 가정함으로써 기체의 압축성을 고려하였다. stream function과 vorticity를 변수로 사용하였으며, 큰 각속도에서도 수치모사의 안정성을 유지하기 위해서 upwind difference 법을 사용하였다. 유도된 차분 방정식을 푸는데는, SOR과 SIP(strongly implicit procedure)를 사용했으며, 후자가 본 system에 대해서 더욱 효율적임을 알았다. 또 SIP를 사용하는 경우 artificial viscosity에 기인하는 오차를 줄이기 위해서 Jacobs 수정법(1974)을 사용했다. 수치모사의 결과로 streamline과 축방향속도 분포, 그리고 분리된 boundary layer와 옆 벽에서의 Stewartson layer에 의한 유체의 흐름을 볼 수 있었다.

수치모사 결과를 검토하기 위해서, 200~500 rpm의 범위로 회전하는 모델실린더를 제작하였다. 실린더의 윗덮개의 중심쪽에 있는 slit를 통해 공기를 불어넣었고, 윗덮개의 바깥쪽과 아랫 덮개에

있는 slit 를 통해 뽑아내었으며, 그 흐름을 관측할 수 있도록 paraffine mist 를 첨가하였다. 이렇게 하여 측정한 축 방향속도를 수치모사의 결과와 비교하였다.

ABSTRACT

Steady axisymmetric source-sink flows of a compressible viscous fluid in a rotating cylinder is simulated numerically. The source and the sink are, respectively, the feed and the discharge slits at the end plates of the cylinder. Compressibility of the fluid is taken into account in the form of steady-state density stratification in the radial direction formed by rigid body rotation in the absence of the source and sink. Stream function-vorticity formulation is chosen for this study. Stability problem ocurring at high angular speed is overcome by using upwind difference scheme.

The solution techniques used for the resulting finite difference equations are SOR and SIP (Strongly Implicit Procedure), and the latter is found to be more efficient for this set of equations. Additionally, when using SIP, we adopted the method devised by Jacobs (1974) to compensate for the error due to the artificial viscosity.

The simulation results give streamlines and axial velocity profiles for the flows through the detached shear layer and the Stewartson layer near the side wall.

To check the results of numerical simulation. a model cylinder was driven at an angular velocity of 200-500r.p.m. The air containing paraffine mist as a tracers is fed into the cylinder through the inlet slit at the upper end plate and is withdrawn through the outlet slits at the upper and lower plates.

Values of axial velocity from the present numerical simulation were compared with those from experiments.

1. Introduction

Dynamics of fluids in a rotating system has been actively investigated in recent years because of its applicability to geophysical flow problems and design of gas centrifuges. One of rotating flow problems which has attracted many people's attention is the axisymmetric flow of a viscous fluid in a rotating cylinder. Attempts have been made to obtain an analytical solution of the velocity field for gases in a rotating cylinder. Parker and Mayo[1], and Ging[2] have obtained such solutions by assuming that the effects of the top and bottom plates are negligible. But in reality the flow pattern is determined not only by the Stewartson layers along the side wall but also by the Ekman layers along the end plates. If we want to take into account both of these boundary layers and the nonlinearity of Navier-Stokes equation, we have to rely on the numerical analysis.

For a complete solution of this problem, energy equation has to be solved together with the Navier-Stokes equation. However, this technique would require large computer memories and tremendous amount of computation time. In the present work, the den-

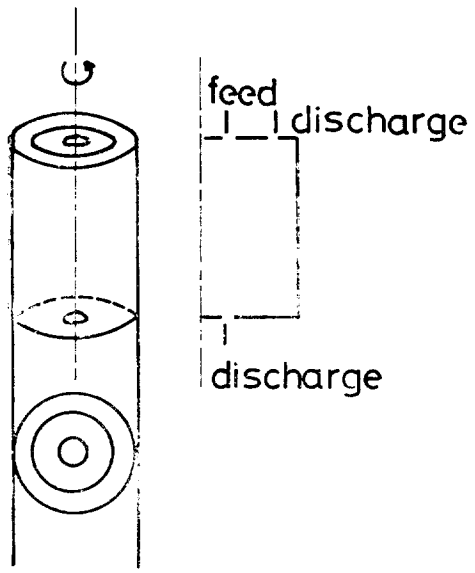

Fig. 1. Description of the System

sity field in the rotating cylinder is assumed identical to that of the rigid body rotation. With this approximation, stream function-vorticity function approach can be adopted. This simulation will accurately give the flow pattern in a rotating cylinder when the feed rate of gas is small.

To check some of the numerical simulation results, model cylinder of 10cm radius and 60 cm height was constructed and axial velocity in the detatched shear layer was measured with cathetometer and stopwatch.

2. Theory

2-1. Mathematical Formulation

The system to be simulated is depicted in *Figure 1*. A circular cylinder with slits on its top and bottom plates is rotating about its axis with a constant angular velocity. These slits, through which gas is allowed to pass into and out of the cylinder, have the role of source and sink of the system. The present analysis is performed under the following assumptions.

(1) The gravitational acceleration is negligibly small compared with the centrifugal acceleration.
(2) The gas is ideal
(3) The system is isothermal
(4) The system is axisymmetric

The governing equation in the reference frame which is rotating at the same angular velocity as the system is as follows.

$$\rho\left(\frac{D\underline{v}}{Dt} + 2\underline{\Omega} \times \underline{v}\right) = -\nabla p + \mu\nabla^2\underline{v} + (\lambda + \mu)\nabla(\nabla.\underline{v}) + \frac{1}{2}\rho\mathrm{grad}(|\underline{\Omega} \times \underline{r}|)^2 \quad (1)$$

Continuity equation in the rotating reference frame is

$$\frac{\partial\rho}{\partial t} + \frac{1}{r}\frac{\partial}{\partial r}(r\rho u) + \frac{\partial}{\partial z}(\rho w) = 0 \quad (2)$$

Next, consider the rigid body rotation of a gas in a cylinder. If there is neither source nor sink, the gas motion is simply a rigid body rotation when steady. In this state, all components of the velocity vector become zero with respect to the rotating frame. Then, Equation (1) is simplified to

$$\nabla\bar{p} = \frac{1}{2}\bar{\rho}\mathrm{grad}\ (|\underline{\Omega} \times \underline{r}|^2) \quad (3)$$

Where the superposed bar means the state of rigid body rotation. That is, the pressure gradient balances the centrifugal force. Substituting $\frac{\bar{p}M}{R_gT}$ for $\bar{\rho}$ (ideal gas assumption), we obtain the following relation for pressure and density distribution.

$$\bar{p} = p_0\exp\left(\frac{M\Omega^2}{2R_gT}r^2\right) \quad (4)$$

$$\bar{\rho} = \rho_0\exp\left(\frac{M\Omega^2}{2R_gT}r^2\right) \quad (5)$$

Where p_0 and ρ_0 are the respective values of p and ρ at the center of the cylinder in the state of rigid body rotation. Equation (5) shows the density distribution in the steady state when there is no source and si-

nk. But when the source and the sink are present, the density field deviates from it. When the feed rate is small, however, the deviation can be neglected and the density distribution approximated by that of the rigid body rotation. Substituting $p=\bar{p}$ and $\rho=\bar{\rho}$, we obtain the equations of motion,

$$\bar{\rho}\left(\frac{D\underline{v}}{Dt}+2\underline{\Omega}\times\underline{v}\right)=\mu\nabla^2\underline{v}+(\lambda+\mu)\nabla(\nabla\cdot\underline{v}) \tag{6}$$

where pressure gradient and centrifugal force terms cancelled out each other. Continuity equation becomes

$$\nabla\cdot(\bar{\rho}\underline{v})=\frac{1}{r}\frac{\partial}{\partial r}(ru\bar{\rho})+\frac{\partial}{\partial z}(\bar{\rho}w)=0 \tag{7}$$

After a rearrangement, we obtain the following continuity equation.

$$\frac{\partial u}{\partial r}+\frac{u}{r}+\frac{\partial w}{\partial z}+\frac{M\Omega^2}{R_gT}(ru)=0 \tag{8}$$

Now we introduce the Stokes' stream function.

$$u=\frac{1}{r\bar{\rho}}\frac{\partial\psi}{\partial z} \tag{9}$$

$$w=-\frac{1}{r\bar{\rho}}\frac{\partial\psi}{\partial r} \tag{10}$$

And define the vorticity (10)

$$\zeta=\frac{\partial u}{\partial z}-\frac{\partial w}{\partial r} \tag{11}$$

and a variable

$$\Gamma=vr \tag{12}$$

From the r-and the z-components of Equation (6), we obtain the following vorticity transport equation.

$$\rho\left[\frac{\partial\zeta}{\partial t}+u\frac{\partial\zeta}{\partial r}+w\frac{\partial\zeta}{\partial z}-\frac{1}{r^3}\frac{\partial\Gamma^2}{\partial z}-\frac{2\Omega}{r}\frac{\partial\Gamma}{\partial z}-\left(\frac{u}{r}+\frac{M\Omega^2}{R_gT}ru\right)\zeta\right]-\frac{M\Omega^2}{R_gT}r\left[-\mu\left(\frac{\partial\zeta}{\partial r}+\frac{\zeta}{r}+\frac{M\Omega^2}{R_gT}r\frac{\partial u}{\partial z}\right)-(\lambda+\mu)\frac{M\Omega^2}{R_gT}r\frac{\partial u}{\partial z}\right]=\mu\left[\nabla^2\zeta+\frac{1}{r}\frac{\partial\zeta}{\partial r}-\frac{1}{r^2}\zeta\right] \tag{13}$$

where $\nabla^2=\frac{\partial^2}{\partial z^2}+\frac{\partial^2}{\partial r^2}$, and the superposed bar has been omitted for brevity. The azimuthal component of the momentum equation becomes, in terms of Γ

$$\rho\left(\frac{\partial\Gamma}{\partial t}+u\frac{\partial\Gamma}{\partial r}+w\frac{\partial\Gamma}{\partial z}+2\Omega ru\right)=\mu\left(\nabla^2\Gamma-\frac{1}{r}\frac{\partial\Gamma}{\partial r}\right) \tag{14}$$

And from the definition of vorticity, we obtain stream function equation

$$\nabla^2\psi-\left(\frac{1}{r}+\frac{M\Omega^2}{R_gT}r\right)\psi_r=\rho r\zeta \tag{15}$$

Introducing the following dimensionless variables,

$$z^*=\frac{z}{R},\quad r^*=\frac{r}{R},\quad t^*=t\Omega$$

$$u^*=\frac{u}{\Omega R},\quad v^*=\frac{v}{\Omega R},\quad w^*=\frac{w}{\Omega R}$$

$$\zeta^*=\frac{\partial u^*}{\partial z^*}-\frac{\partial w^*}{\partial r^*}=\frac{\zeta}{\Omega},\quad \Gamma^*=r^*v^*=\frac{\Gamma}{\Omega R^2}\quad \rho^*=\frac{\rho}{\rho^0}=\exp\left(\frac{M\Omega^2R^2}{2R_gT}r^{*2}\right),$$

$$\psi^*=\frac{\psi}{\rho_0\Omega R^3}\quad \nu=\frac{\mu}{\rho_0},\quad Re=\frac{\Omega R^2}{\nu}$$

$$G=\frac{M\Omega^2R^2}{R_gT},\quad V=\frac{\lambda+\mu}{\mu}=\frac{1}{3}$$

(Stokes' hypothesis) (16)

and omitting the asterisks for brevity, we obtain a new set of governing equations,

$$\frac{\partial\Gamma}{\partial t}+u\frac{\partial\Gamma}{\partial r}+w\frac{\partial\Gamma}{\partial z}+2ru=\frac{1}{Re\rho}\left(\nabla^2\Gamma-\frac{1}{r}\frac{\partial\Gamma}{\partial r}\right) \tag{17}$$

$$\frac{\partial\zeta}{\partial t}+u\frac{\partial\zeta}{\partial r}+w\frac{\partial\zeta}{\partial z}-\frac{1}{r^3}\frac{\partial\Gamma^2}{\partial z}-\frac{2}{r}\frac{\partial\Gamma}{\partial z}-\frac{u}{r}\zeta-Gru\zeta=-\frac{G}{Re\rho}\left(r\frac{\partial\zeta}{\partial r}+\zeta+Gr^2\frac{\partial u}{\partial z}+VGr^2\frac{\partial u}{\partial z}\right)+\frac{1}{Re\rho}\left(\nabla^2\zeta+\frac{1}{r}\frac{\partial\zeta}{\partial r}-\frac{\zeta}{r^2}\right) \tag{18}$$

$$\nabla^2\psi-\left(\frac{1}{r}+Gr\right)\psi_r=\zeta r\rho \tag{19}$$

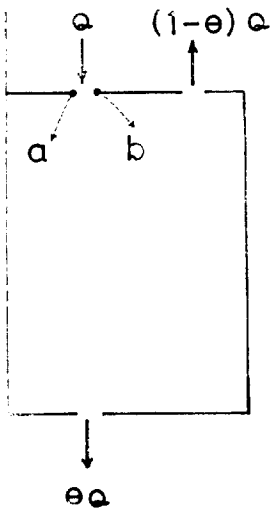

Fig. 2. Determination of Boundary Conditions

The equations (1)-(19) are generally valid for unsteady states. Even though we consider only the steady state in the following calculations, the time derivatives $\partial\Gamma/\partial t$ and $\partial\zeta/\partial t$ have been retained in the above for future applications. Boundary conditions for these equations are postulated in the following manner. On the symmetric axis shown in *Fig. 2*, we have $\psi = 0$ and $\zeta = 0$. From the definition of the stream functions, we get

$$\psi_b - \psi_a = -\int_a^b \rho r w dr = \frac{Q}{2\pi}$$

Taking $\psi_a = 0$, we can write $\psi_b = Q/2\pi$. Since the paths of the gas through the slits are very short in actual geometry, the flow is not expected to be fully developed. Thus, we make the simplest possible speculation by assuming plug flow of the gas through the slits. This gives the constant gas velocity

$$w = -\frac{(Q/2\pi)G}{\exp\left(\frac{1}{2}Gr_b^2\right) - \exp\left(\frac{1}{2}Gr_a^2\right)} \qquad (20)$$

at the feed slit. The treatment is similar for the discharge slits.

For the boundary values of vorticity, we take the following form, which is most frequently used and, in fact, most stable.[5]

$$\zeta_w = \frac{2(\psi_{w+1} - \psi_w)}{(\Delta r)^2} \qquad (21)$$

where subscript w denotes the no slip wall and Δr is the distance from $w+1$ to w, normal to the wall.

2-2. Numerical Schemes

There are two approaches to numerical fluid dynamics. That is to say, asymptotic approach(time dependent approach) and steady state approach.

In the asymptotic approach, we solve the governing equations from initial time($t = 0$) and repeat the procedure at each time step as time is increased until steady-state is attained. But when we use steady state approach, time derivative terms are dropped at the start and the resulting elliptic equations are solved by the available standard methods.

Here, we employ steady state approach and the finite difference equations are solved by the successive over-relaxation method and the strongly implicit procedure.

Let the finite difference discretization of the steady state from of the governing equations be

$$\underset{\sim}{A}\underset{\sim}{\phi} = \underset{\sim}{S} \qquad (22)$$

where $\underset{\sim}{\phi}$ is the solution vector which may be azimuthal velocity, vorticity or stream funciton. The matrix $\underset{\sim}{A}$ is pentadiagonal if the five point formula for the Laplacian operator is adopted. Because of its large dimension, iterative inversion technique is generally employed. A general iteration formula for Equation (22) may be obtained by adding an auxiliary term $\underset{\sim}{A}$ to each side of Equation (22) and putting the iteration nu-

mbers to ϕ as

$$(\underset{\sim}{A}+\tilde{\underset{\sim}{A}})\underset{\sim}{\phi}^{(N)}=\tilde{\underset{\sim}{A}}\underset{\sim}{\phi}^{(N-1)}+\underset{\sim}{S} \quad (23)$$

where N is the number of the iterations, and $\tilde{\underset{\sim}{A}}$ is chosen so that the inversion of $(\underset{\sim}{A}+\tilde{\underset{\sim}{A}})$ may become easy. The convergence rate becomes faster as $\tilde{\underset{\sim}{A}}$ becomes close to $\underset{\sim}{Q}$. The techniques employed in this study are SOR(Successive Over-Relaxation)and SIP (Strongly Implicit Procedure). The SOR scheme is

$$\tilde{\underset{\sim}{A}}=(1-w)\ \underset{\sim}{L}+\underset{\sim}{U} \quad (24)$$

$$\underset{\sim}{\phi}^{(N)}=(\underset{\sim}{D}-w\underset{\sim}{L})^{-1}\ [(1-w)\underset{\sim}{D}+w\underset{\sim}{U}]$$
$$\underset{\sim}{\phi}^{(N-1)}+(\underset{\sim}{D}-w\underset{\sim}{L})^{-1}w\underset{\sim}{S} \quad (25)$$

where w is the relaxation parameter to be determined computationally, and $\underset{\sim}{L}$ and $\underset{\sim}{U}$ are lower and upper triangular matrices respectively. In the SIP[3,4] $\tilde{\underset{\sim}{A}}$ is chosen so that $(\underset{\sim}{A}+\tilde{\underset{\sim}{A}})$ can be factorized as

$$\underset{\sim}{A}+\tilde{\underset{\sim}{A}}=\underset{\sim}{L}\cdot\underset{\sim}{U} \quad (26)$$

Because of the nature of $\underset{\sim}{L}$ and $\underset{\sim}{U}$ the inversion of $\underset{\sim}{L}\cdot\underset{\sim}{U}$ is easily done. Additionally the auxiliary matrix $\tilde{\underset{\sim}{A}}$ for SIP is very small, from which the name "strongly implicit" originates.

2-3. Upwind differencing and Jacobs' Correction Method

For a successful iteration scheme(Equation (23)), the matrix $\underset{\sim}{A}$ of the coefficients of finite difference equations, should be irreducible and diagonally dominant. For high Reynolds number (in the present case, high angular velocity), the matrix get out of diagonal dominance. To remedy this difficulty, upwind difference scheme is used for azimuthal velocity equation and vorticity transport equation. But the upwind difference scheme is accurate only up to the first order in Δx. The second order error, called artificial viscosity, increases with the Reynolds number[5]. Recently Jacobs proposed a correction method[6] for it. The set of finite difference equations resulting from centered difference scheme, which is accurate up to the second order, is represented by, in a matrix form

$$\underset{\sim}{A}\underset{\sim}{\phi}=\underset{\sim}{S} \quad (27)$$

and the equation resulting from upwind difference scheme by

$$\underset{\sim}{A}'\underset{\sim}{\phi}=\underset{\sim}{S}'$$
$$=\underset{\sim}{S}-(\underset{\sim}{A}-\underset{\sim}{A}')\underset{\sim}{\phi} \quad (28)$$

The term $(\underset{\sim}{A}-\underset{\sim}{A}')\underset{\sim}{\phi}$ represents the second order error introduced by using upwind difference scheme. We form the matrices $\underset{\sim}{L}$ and $\underset{\sim}{U}$ in a way such that

$$\underset{\sim}{L}\cdot\underset{\sim}{U}=\underset{\sim}{A}'+\tilde{\underset{\sim}{A}}' \quad (29)$$

That is, we use matrix $\underset{\sim}{A}'$ instead of the matrix $\underset{\sim}{A}$ to determine the factorization matrices $\underset{\sim}{L},\underset{\sim}{U}$.

The iteration scheme is derived as follows.

$$\underset{\sim}{A}\underset{\sim}{\phi}=\underset{\sim}{S}$$

Adding both sides $\tilde{\underset{\sim}{A}}'\underset{\sim}{\phi}$, and adding and sub tracting the term $\tilde{\underset{\sim}{A}}'\underset{\sim}{\phi}$ in the left hand side, we find

$$(\underset{\sim}{A}'+\tilde{\underset{\sim}{A}}')\underset{\sim}{\phi}^{(N+1)}+(\underset{\sim}{A}-\underset{\sim}{A}')\underset{\sim}{\phi}^{(N)}=\tilde{\underset{\sim}{A}}'\underset{\sim}{\phi}^{(N)}$$
$$+\underset{\sim}{S} \text{ i.e.} \quad (30)$$

$$(\underset{\sim}{A}'+\tilde{\underset{\sim}{A}}')\ (\underset{\sim}{\phi}^{(N+1)}-\underset{\sim}{\phi}^{(N)})=\underset{\sim}{S}-\underset{\sim}{A}\underset{\sim}{\phi}^{(N)}$$
$$\underset{\sim}{L}\underset{\sim}{U}\delta\underset{\sim}{\phi}^{(N)}=-\underset{\sim}{R}^{(N)} \quad (31)$$

where $\underset{\sim}{L}\underset{\sim}{U}=\underset{\sim}{A}'+\tilde{\underset{\sim}{A}}'$ and $\delta\underset{\sim}{\phi}^{(N)}=\underset{\sim}{\phi}^{(N+1)}-\underset{\sim}{\phi}^{(N)}$. Accordingly, when we compute factorization matrices $\underset{\sim}{L}$ and $\underset{\sim}{U}$, we use matrix $\underset{\sim}{A}'$ thus ensuring stability. And, when we compute the residue vector $\underset{\sim}{R}$, we use matrix $\underset{\sim}{A}$, causing the iteration not to cease until second order accurate solution of centered differencing is obtained. Additionally we introduced a relaxation factor to avoid the diverging of iteration scheme.

$$\underset{\sim}{L}\underset{\sim}{U}\delta\underset{\sim}{\phi}^{(N)}=-w\underset{\sim}{R}^{(N)}$$

This relaxation factor was not proposed in the Stone's original paper[3]. Finite diffe-

rence discretizations of the governing equations are presented in the appendix. Here, the convergence of the solution for Γ,ζ and ψ was considered to have occurred when the maximum relative error for each stream function is less than ε. Namely,

$$\max \left| \frac{\psi^{N}_{ij} - \psi^{N-1}_{ij}}{\psi_{ij}} \right| < \varepsilon \qquad (32)$$

where ε is about 10^{-4}. It has been observed that ψ is more sensitive than the other two variables. In other words, when the stream function distribution satisfies Equation (32), the ζ and Γ distributions are also found to satisfy the analogous convergence criteria.

3. The System for Numerical Simulation

The particular problems of our interest concern the rotation of a cylinder when its radius R is 9cm and its height H ranges from 20 to 60 cm. Thus the aspect ratio H/R varies from 2.2 to 6.67. The inlet slit is located at 2.5cm from the axis of revolution on the top plate and the outlet slits located at 8.0cm from the center on the top plate and 2.5 cm from the center on the bottom plate.

The cut ratio, θ is allowed to vary from 1.0 (no flow to the outlet slit on the top plate) to 0.5. The properties of the gas are similar to that of the air at 25°C.

The density and the viscosity of air at this temperature are 1.295×10^{-3} g/cm^3 and 0.0182 cp. respectively. Air is introduced at the rate of 3-12 g/min and the angular speed of the cylinder varies between 50 r.p.m. and 10,000 r.p.m The finite difference computations are carried out according to the conventional procedure,[7] using Cyber-174.

4. Experimental

4-1. Experimental Apparatus

To check the results of numerical simulation, a model cylinder of radius 6cm and height 60cm was constructed. It was driven in the air by a variable speed $\frac{1}{4}$ hp motor at 200-500 r.p.m.

A schematic diagram of the experimental setup is shown in *Fig. 8*. It consists of a rotating cylinder, its base frame, paraffine mist generator and flowmeters. The side wall of the cylinder is made of transparent, 1-cm thick acryl plates, and the top and bottom plates are fabricated with aluminium to make the cylinder lighter.

The feed slit is located on the top plate at the relative radius of 0.278. One discharge slit is located on each plate; at the relative radius of 0.889 on the top plate and at 0.278 on the bottom plate. The air is supplied by a pressurized container, fed into the cylinder through the feed slit on the top plate and discharged from the discharge slits on both plates. The cut θ, which denotes the fraction of feed through the bottom discharge slit, is controlled by the valves on the discharge lines.

To visualize the motion of the air, mist of liquid paraffine is added to the feed intermittently. Paraffine mist is made in the paraffine mist generator. Unlike the commonly used Preston-Sweeting paraffine mist generator, a heating coil is immersed directly into the liquid paraffine to generate sufficient amount of mist here. By controlling the electric current from the power

supply to coil, the mist is introduced into the air stream intermittently. The streamlines are most clearly visualized near the detached shear layer located at the radial position coinciding with the feed slit, and the axial velocity of this boundary layer was measured at each axial position.

A stroboscope was used to measure the angular speed of the rotating cylinder.

4-2. Experimental Procedure

(1) Determine angular speed of the cylinder with the aid of stroboscope.

(2) Open the valve of air regurator and wait until the flow reaches the steady state. Feed flow rate is controlled by the valve on the feed line.
Adjust the valves on the discharge line so that the cut reaches the desired value.

(3) Connect heating coil with the power source, thus making liquid paraffine evaporate.

(4) When the front of air stream burdened with paraffine mist approaches the axial position where the measurement is desired, the axial velocity is measured with the cathetometer and stop-watch. In advance, the optical part of the cathetometer is arranged to move up and down a certain interval, at the center of which is located the point of measurements. Actually this interval was 10 cm, that is, ±5cm from the center.

(5) Disconnect heating coil from the power source such that only air is fed into the cylinder. Wait until the paraffine mist is completely discharged from the cylinder. By this moment, all parts of the cylinder are clearly visible. Repeat the procedure (1)-(5) changing r.p. m., feed flow rate, etc.

5. Results and Discussion

5-1. Discussion of the Numerical Scheme

Optimum parameter of SOR was determined computationally. For low angular velocity(less than 500 r.p.m.), the values of this parameter were found to lie in the range of 1.2-1.6, and this value decreased as the angular speed increased. When the angular speed was 10,000 r.p.m., the relaxation parameter decreased to the order 0.01 for vorticity transport equation and the number of iterations required for convergence was approximately 2,000 for 20 x 20 meshes.

Since we adopted non-uniform mesh structure, the mesh was mostly rectangular rather than square. It was found that this tended to make the numerical procedure relatively unstable, thus requiring the relaxation parameter to have smaller values than the square mesh for the stabilization of the numerical scheme. The instability arises probably from the round-off error due to excessive divisions by small numbers.

It was also found that the convergence rate also decreased as the number of mesh increased.

Besides SOR,a new strongly implicit iterative method, SIP was used. In this case, we iterated the scheme 4 times for each equation using the sequence of Stone's iteration parameter α. These iteration parameters were spaced geometrically as suggested by Stone[3]

$$1-\alpha_l=(1-\alpha_{\max})^{l/(L-1)},\quad l=0,1,\cdots,L-1$$

where L is the number of parameters in a cycle and $\alpha_{\max}$ is the maximum iteration parameter. The value of $\alpha_{\max}$ was taken as

$$1-\alpha_{max}=\min\left\{\frac{2(\Delta r)^2}{1+\frac{(\Delta r)^2}{(\Delta z)^2}},\ \frac{2(\Delta z)^2}{1+\frac{(\Delta z)^2}{(\Delta r)^2}}\right\}$$

If α_{max} is too large, the iteration scheme diverges and we have to reduce α_{max}. However, if it is too small, the convergence becomes proportionally slow. The appropriate value of α_{max} is determined computationally in the end. For a high angular velocity or for a mesh aspect ratio far different from 1 (say, about 6), α_{max} has to be as smll as 0.6 so that the system can converge. In addition to the iteration parameter, it was necessary to introduce the relaxation parameter ω with values in the range of 0-1. This parameter was not proposed in the Stone's original paper. This may be due to the fact that his model equation was the heat conduction equation with variable therm al conductivity. The equation for the nonlinear heat conduction is much more moderate than the nonlinear Navier- Stokes equation in the degree of nonlinearity. Typical values of this relaxation parameter are about 0.5 for 500 r.p.m. and 0.01 for 10,000 r.p.m. for vorticity transport equation. The other two equations for the azimuthal velocity and the stream function can have a little larger values for the relaxation parameter than the vorticity transport equation can. When using Jacob's correction method, we must choose for this relaxation parameter a value smaller than that for a simple SIP to attain the stability.

The rectangular grid systems, particularly the nonuniform, lead to instabilities for SIP as for SOR, but it is severer for SIP than for SOR. In order to succeed in iteration, it was necessary to make the values of the relaxation parameter smaller than the square grid systems.

In general, simple SIP was found to be 2-3 times as fast as SOR iteration. When Jacob's correction was taken into the SIP, additional time required over simple SIP was about 20% more at 10,000 r.p.m. The comparison of computer time required for simple SIP and SOR is shown in **Table.** *1.*

The model equation is the set of our governing equations (Equations 17, 18 and 19) with the uniform grid of 10 x 10.

Table 1. Comparison of computing time between simple SIP and SOR

r.p.m	#of outer iteration in SIP	in SOR	ratio of computing time SIP/SOR
50	12	321	0.74
500	18	658	0.55
10,000	46	2,210	0.41

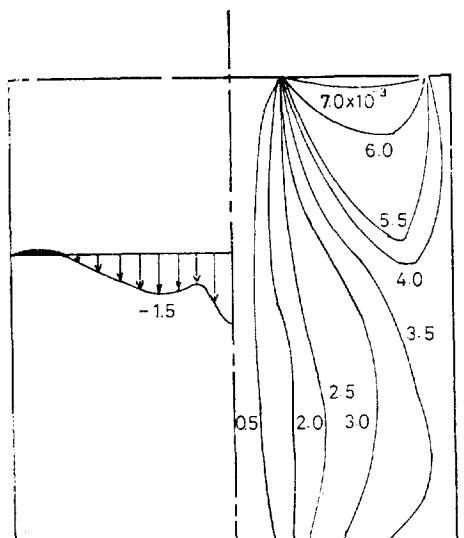

Fig. 3. Axial Velocity Profile and Streamlines $Q = 3g/min$, $\theta = 0.5$, $\Omega = 2,000$ r.p.m. $H/R = 6$

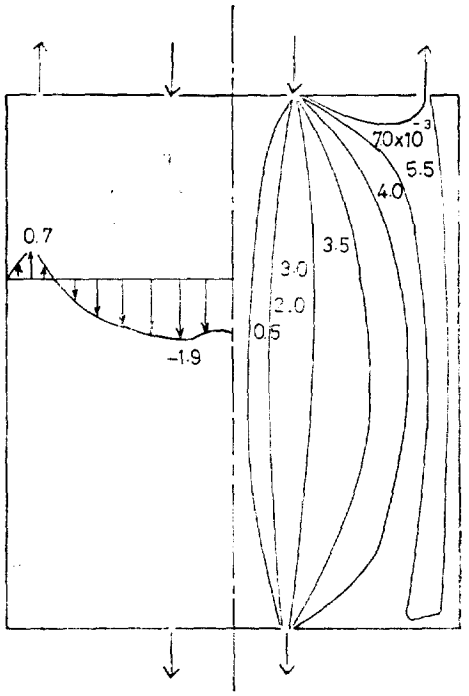

Fig. 4. Axial Velocity Profile and Streamlines
$Q = 3$g/min, $\theta = 0.5$, $\Omega = 10,000$ r.p.m.,
H/R = 6

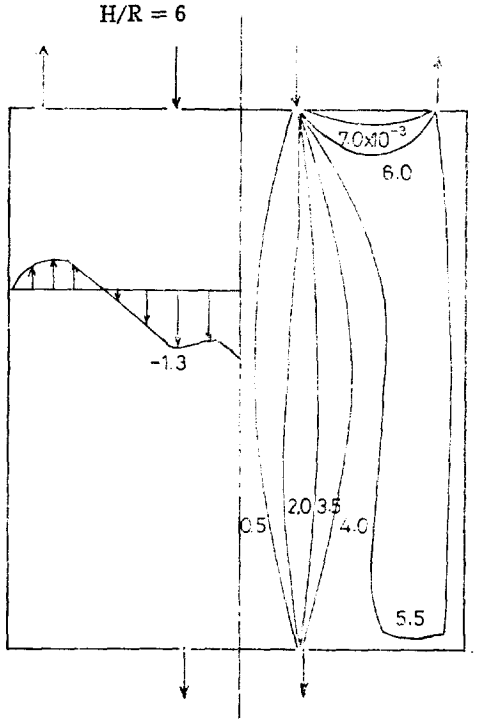

Fig. 5. Axial Velocity Profile and Streamlines
$Q = 3$g/min, $\theta = 0.5$, $\Omega = 2,000$ r.p.m.,
H/R = 3

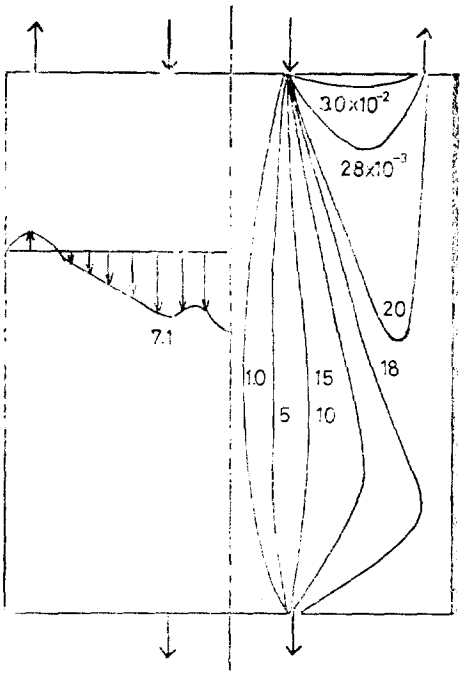

Fig. 6. Axial Velocity Profile and Streamlines
$Q = 12$g/min, $\theta = 0.5$, $\Omega = 2,000$ r.p.m.,
H/R = 6

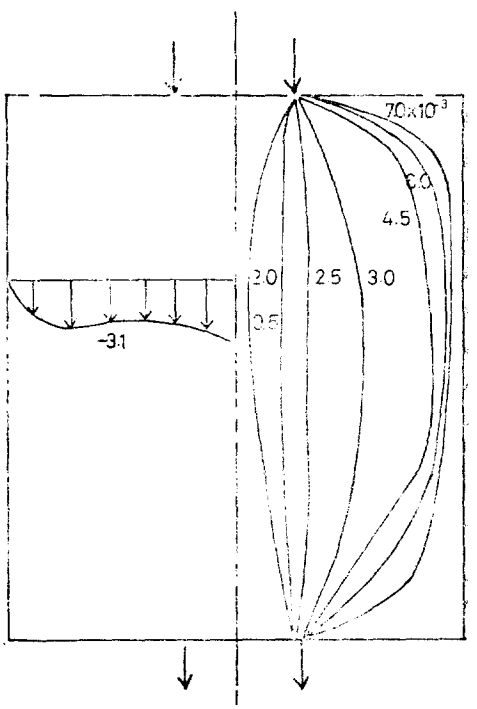

Fig. 7. Axial Velocity Profile and Streamlines
$Q = 3$g/min, $\theta = 1.0$, $\Omega = 2,000$r.p.m.,
H/R = 6

5-2. Results

Streamlines and axial velocity profiles at the relative axial position of 1/3 from the top plate for various feed flow rates, the cut ratio θ, angular velocities and the cyl inder aspect ratio H/R are shown in *Fig. 3* through *7*. All contours were obtained by linear interpolation of the nodal point values.

Fig. 3 and *4* show the axial velocity profile and streamlines when the cylinders with the aspect ratio of 6 are rotating at two different angular velocities (2,000 r.p.m. for *Fig. 3* and 10,000 r.p.m. for *Fig. 4*) Air is introduced at the rate of 3g/min to the top slit and discharged through the slits on the bottom and on the top plates ($\theta = 0.5$). It is seen that rechanneling flow approaches nearer to the side wall and to the bottom plates as the angular speed increases. *Fig. 5* shows the results when the aspect ratio is reduced from 6 (*Fig. 3*) to 3 while other conditions remain the same as in *Fig. 3*. Rechanneling flows come down to the bottom plate even at a lower angular speed (2,000 r.p.m.) *Fig. 6* shows the results when the air feed rate is increased to 12g/min in comparison with the conditions given in *Fig. 3* (3g/min). *Fig. 7* shows that the streamlines are crowded toward the wall than at other locations in the cylinder when all of the gas is discharged through the bottom slit ($\theta = 1.0$). In this case, there are two main routes of flow. One route is the detached boundary layer and the other is the Stewartson layer on the side wall. Axial velocities in the detached shear layer are shown in *Fig. 9*. They take the shape of plateau in the middle section of the cylinder.

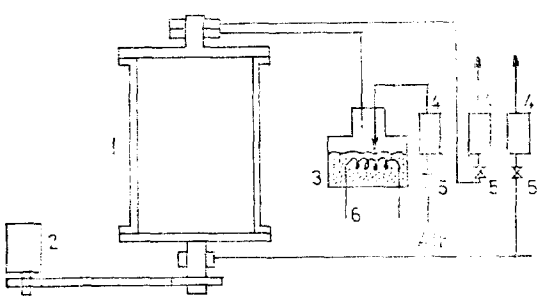

1. rotating cylinder
2. variable speed motor
3. paraffine mist generator
4. flowmeter
5. check valve
6. heating coil

Fig. 8. Schematic Diagram of Experimental Apparatus

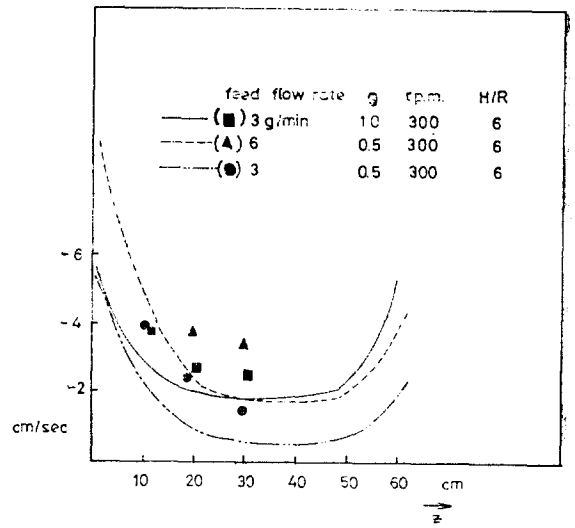

Fig. 9. Axial Velocity in the Detached Shear Layer (Lines represent the computational values and ●, ▲, ■ are from the experiments.)

Values of the axial velocity from our experiment are compared with those from numerical simulation in *Fig. 9*.

In this figure, solid lines are values from numerical simulation and dots are values from experiment.

As previously explained, these experimental values are the average value of the

axial velocity in the axial interval of 10cm centering the indicated point.

Common to all these cases, the absolute value of axial velocity obtained from experiment is somewhat larger than that from simulation. All data show about 1cm/sec higher values than predicted. It appears to be due to a systematic error in the measurement. The main cause of this deviation is attributed to the difficulties associated with the measurements of the velocity in a rotating frame and the use of relatively crude technique for it. We believe, however, that the experiment sufficiently demonstrates the general pattern predicted by the numerical analysis. The density stratification of air estimated by Equation (5) is almost negligible in this numerical experiment. Namely, When we assume the rigid body rotation of air in the cylinder, the air at the wall is only 0.2% heavier than the one in the center for 2,000 r.p.m. and 5.2% for 10,000 r.p.m. in the geometries used for this investigation.

6. Conclusion

Source-sink flow in a rotating cylinder has been simulated numerically and axial velocity measured experimentally to demonstrate the result of the simulation. Under the assumption that the density distribution is the same as that in the rigid body rotation, stream function—vorticity formulation has been attempted. The resulting equations have been discretized and solved by SOR and SIP. Experimentally determined axial velocities have been compared with those of simulation, which tended to have larger values than the simulation in all cases.

Major results are summarized as follows.

(1) SIP is more efficient than SOR for the present system.

(2) Numerical error due to artificial viscosity is eliminated by using Jacob's corrected form of SIP.

(3) In SIP, the relaxation parameter must be introduced in addition to Stone's iteration parameter to ensure stability.

(4) As the angular velocity increases, the rechanneling flow approaches nearer to the side wall and to the bottom plate.

(5) Axial velocity profile takes the shape of plateau in the middle part of the cylinder.

Nomenclature

Roman letters

$\underset{\sim}{A}$ matrix formed by finite difference discretization

$\underset{\sim}{D}$ diagonal matrix decomposed from matrix $\underset{\sim}{A}$

$\underset{\sim}{L}$ lower triangular matrix formed from matrix $\underset{\sim}{A}$

H height of a cylinder, (cm)

P pressure

R radius of a cylinder, (cm)

r variable in the radial direction of the cylindrical coordinate, (cm)

Q feed flow rate, (g/min)

R_g gas constant, 8.3×10^7 (g cm^2 sec^{-2} g-$mole^{-1}$ k^{-1})

t time

u radial velocity, (cm/min)

$\underset{\sim}{U}$ upper triangular matrix formed from matrix $\underset{\sim}{A}$

v azimuthal velocity, (cm/min)

w axial velocity, (cm/min)

z variable in the axial direction of the cylindrical coordinate, (cm/min)

Greek letters

α_i Stone's iteration parameter
ϵ relative error tolerance
ζ vorticity
θ cut ratio
λ second viscosity coefficient
μ viscosity
ν kinematic viscosity, (cm^2/sec)
ψ stream function,
ρ density, (g/cm^3)
Ω angular velocity, (rad/sec) or r.p.m.
Γ rv

Subscript

$\sim$ vector
$\approx$ matrix

Supercript

— the state of rigid body rotation
* dimensionless variable
° quantities with respect to the fixed frame of reference

Operators

Δ difference operator
∇ gradient vector
∇^2 Laplacian operator
$\frac{D}{Dt}$ substantial derivative

Acknowledgements

We wish to thank the KIST for allowing our use of its laboratory facilities and computers.

References

1. H.M. Parker and T.T. Mayo, UVA-279-63 u (1963).
2. J. Ging, U.S. AEC Rep. UVA-198-62s (1962).
3. H.L. Stone, SIAM, J. Numer. Anal., 5 (1968), 530.
4. H.G. Weinstein, H.L. Stone and T.V. Kwan, Society of Petroleum Engineers Journal, June (1970), 99.
5. R.J. Roache, "Computational Fluid Dynamics", Hermosa, Albuquerque, 1972.
6. D.A.H. Jacobs, in "Numerical Methods in Fluid Dynamics.", Eds. C.A. Bebbia and J.J. Connor, Pentech. Press, 1974.
7. A.D. Gosman, W.M. Pun, A.K. Runchall, D.B. Spalding and M.W. Wolfstein, "Heat and Mass Transfer in Recirculating Flow.", Academic Press, London, 1969.
8. D.J. Tritton, "Physical Fluid Dynamics.", Van Nostrand Reinhold, NewYork, 1977.

Appendix

The steady state form of governing equations in the finite difference form are formulated as follows.

(i) Azimuthal velocity equation

$$u_{ij}\left(A_2\frac{\Gamma_{ij}-\Gamma_{i-1,j}}{h_{i-1}}+A_3\frac{\Gamma_{i+1,j}-\Gamma_{ij}}{h_i}\right)+w_{ij}\left(A_4\frac{\Gamma_{ij}-\Gamma_{i,j-1}}{k_{j-1}}+A_5\frac{\Gamma_{i,j+1}-\Gamma_{ij}}{k_j}\right)+2r_iu_{ij}=\frac{1}{R_e\rho_i}\left[k_{Ri}''\Gamma_{i+1,j}-k_{Ci}''\Gamma_{ij}+k_{Li}''\Gamma_{i-1,j}+k_{Rj}''\Gamma_{i,j+1}-k_{Cj}''\Gamma_{ij}+k_{Lj}''\Gamma_{i,j-1}-\frac{1}{r_i}\left(h_{Ri}'\Gamma_{i+1,j}+h_{Ci}'\Gamma_{ij}-h_{Li}'\Gamma_{i-1,j}\right)\right]$$

(ii) Vorticity transport equation

$$u_{ij}\left(A_2\frac{\zeta_{ij}-\zeta_{i-1,j}}{h_{i-1}}+A_3\frac{\zeta_{i+1,j}-\zeta_{ij}}{h_i}\right)+w_{ij}\left(A_4\frac{\zeta_{ij}-\zeta_{i,j-1}}{k_{j-1}}+A_5\frac{\zeta_{i,j+1}-\zeta_{i,j}}{k_j}\right)-\frac{2}{r_i^3}\Gamma_{ij}\left(k_{Rj}'\Gamma_{i,j+1}+k_{Cj}'\Gamma_{ij}-k'_{Lj}\Gamma_{i,j-1}\right)-\frac{2}{r_i}\left(k_{Rj}'\Gamma_{i,j+1}+k_{Cj}'\Gamma_{ij}-k_{Lj}'\Gamma_{i,j-1}\right)$$

$$-\frac{1}{r_i}u_{ij}\zeta_{ij}-Gru_{ij}\zeta_{ij}=-\frac{G}{R_e\rho_i}$$
$$\{r_i(h_{Ri}'\zeta_{i+1,j}+h_{Ci}'\zeta_{i,j}-h_{Li}'\zeta_{i-1,j})+\zeta_{ij}$$
$$+Gr_i^2(k_{Rj}'u_{i,j+1}+k_{Cj}'u_{ij}-k_{Lj}'u_{i,j-1})$$
$$+VGr_i^2(k_{Rj}'u_{i,j+1}+k_{Cj}'u_{ij}-k_{Lj}'u_{i,j-1})\}$$
$$+\frac{1}{R_e\rho_i}\{(h_{Ri}''\zeta_{i+1,j}-h_{Ci}''\zeta_{ij}+h_{Li}''\zeta_{i-1,j})$$
$$+(k_{Rj}''\zeta_{i,j+1}-k_{Cj}''\zeta_{ij}+k_{Lj}\zeta''_{i,j-1})$$
$$+\frac{1}{r_i}(h_{Ri}'\zeta_{i+1,j}+h_{Ci}'\zeta_{ij}-h_{Li}'\zeta_{i-1,j})$$
$$-\frac{1}{r_i^2}\zeta_{ij}\Big\}$$

(iii) Stream function equation

$$h_{Ri}''\phi_{i+1,j}-h_{Ci}''\phi_{ij}+h_{Li}''\phi_{i-1,j}+k_{Rj}''\phi_{i,j+1}$$
$$-k_{Cj}''\phi_{ij}+k_{Lj}''\phi_{i,j-1}-\left(\frac{1}{r_i}+Gr_i\right)$$
$$(h_{Ri}'\phi_{i+1,j}+h_{Ci}'\phi_{ij}-h_{Li}'\phi_{i-1,j})=\zeta_{ij}r_ie_i$$

in which

$A_2=1$ $A_3=0$ for $u_{ij}\geqslant 0$
$A_2=0$ $A_3=1$ for $u_{ij}<0$
$A_4=1$ $A_5=0$ for $w_{ij}\geqslant 0$
$A_4=0$ $A_5=1$ for $w_{ij}<0$

and,

$$h_{Ri}'=\frac{h_{i-1}}{h_i(h_{i-1}+h_i)},\quad h_{Ci}'=\frac{h_i-h_{i-1}}{h_ih_{i-1}},$$
$$h_{Li}'=\frac{h_i}{h_{i-1}(h_{i-1}+h_i)}$$
$$h_{Ri}''=\frac{2}{h_i(h_{i-1}+h_i)},\quad h_{Ci}''=\frac{2}{h_ih_{i-1}},$$
$$h_{Li}''=\frac{2}{h_{i-1}(h_i+h_{i-1})}$$
$$k'_{Rj}=\frac{k_{j-1}}{k_j(k_{j-1}+k_j)},\quad k_{Cj}'=\frac{k_j-k_{j-1}}{k_jk_{j-1}},$$
$$k_{Lj}'=\frac{k_j}{k_{j-1}(k_{j-1}+k_j)}$$
$$k_{Rj}''=\frac{2}{k_j(k_{j-1}+k_j)},\quad k_{Cj}''=\frac{2}{k_jk_{j-1}},$$
$$k_{Lj}''=\frac{2}{k_{j-1}(k_j+k_{j-1})}$$

where h_i and k_j denote grid spacing in the r-direction and z-direction respectively. If centered difference scheme is used, all of the convective terms are changed in the following way.

$$u\frac{\partial\Gamma}{\partial r}\Rightarrow u_{ij}(h_{Ri}'\Gamma_{i+1,j}+h_{Ci}'\Gamma_{ij}-h_{Li}'\Gamma_{i-1,j})$$

etc.